JACS
JOURNAL OF THE AMERICAN CHEMICAL SOCIETY
Article
Cite This: J. Am. Chem. Soc. XXXX, XXX, XXX−XXX
pubs.acs.org/JACS

Uniform Nucleation of Lithium in 3D Current Collectors via Bromide Intermediates for Stable Cycling Lithium Metal Batteries

Hui Duan,[†,∥,⊥] Jing Zhang,[‡,∥,⊥] Xiang Chen,[§,⊥] Xu-Dong Zhang,[†] Jin-Yi Li,[†,∥] Lin-Bo Huang,[†,∥] Xing Zhang,[†] Ji-Lei Shi,[†] Ya-Xia Yin,[†,∥] Qiang Zhang,[§] Yu-Guo Guo,*[,†,∥] Lang Jiang,*[,‡] and Li-Jun Wan*[,†,∥]

[†]CAS Key Laboratory of Molecular Nanostructure and Nanotechnology, CAS Research/Education Center for Excellence in Molecular Sciences, Beijing National Laboratory for Molecular Sciences (BNLMS), Institute of Chemistry, Chinese Academy of Sciences (CAS), Beijing 100190, China

[‡]CAS Key Laboratory of Organic Solids, CAS Research/Education Center for Excellence in Molecular Sciences, Beijing 100190, China

[§]Beijing Key Laboratory of Green Chemical Reaction Engineering and Technology, Department of Chemical Engineering, Tsinghua University, Beijing 100084, China

[∥]University of Chinese Academy of Sciences, Beijing 100049, China

Supporting Information

ABSTRACT: The conductive framework is generating considerable interest for lithium metal anodes to accommodate Li^+ deposition, due to its ability to reduce electrode current density by increasing the deposition area. However, in most cases, the electroactive surface area is not fully utilized for the nucleation of Li in 3D current collectors, especially under high current densities. Herein, uniform nucleation of Li in the conductive skeleton is achieved by a two-step synergetic process arising from CuBr- and Br-doped graphene-like film. The modified electrode regulates Li nucleating in uniform pancake-like seeds and growing into a granular Li metal ascribed to the excellent lithiophilicity of CuBr- and Br-doping sites and the low Li diffusion barrier on the surface of generated LiBr, as confirmed by the experimental and computational results. Therefore, the modified anode endows small nucleation overpotential, a high-reversibility Li plating/stripping process, and excellent performance in full batteries with industrially significant cathode loading. This work suggests that a two-step cooperative strategy opens a viable route to the development of a Li anode with high reversibility for stable cycling Li metal batteries.

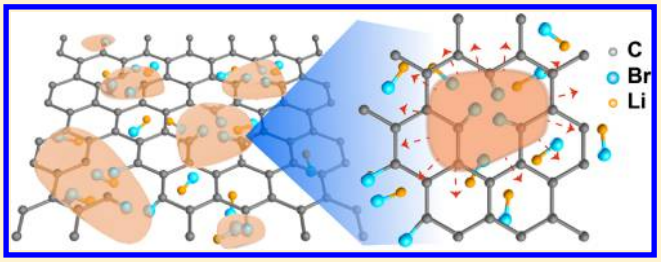

INTRODUCTION

Lithium metal offers access to Li−sulfur and Li−air batteries, thereby promising high energy densities for rechargeable Li batteries.[1−5] However, Li metal is plagued with several unfavorable drawbacks, such as virtually infinite volume change, poor cycle life, and severe safety issues induced by demonic Li dendrites, which are unavoidably formed in rechargeable batteries.[6−9] For decades, diverse efforts have been devoted to addressing the challenging dendrite issues, including various electrolyte additives,[10−14] artificial protection layers on the surface of the Li metal,[15−17] high lithium salt concentrations,[18,19] and solid-state electrolytes.[20−25] Moreover, current density has a significant influence on dendrite formation and growth. The serious dendrite growth at high current density is the key hurdle that must be overcome for practical Li metal anodes.[26] However, previous studies have shown that dendrite growth can be effectively delayed only at a relatively low current density. Additionally, the spatially uncontrolled Li deposition in the "hostless" Li metal at high areal capacity is a huge challenge. Most recently, high-surface-area current collectors have been proposed to accommodate Li^+ deposition for Li metal anodes by reducing local current density. Apart from that, the host used in these reports can provide free space for storing metallic Li to mitigate the volume change during the Li plating/stripping process.[27−30] However, the inhomogeneous Li^+ flux distribution and mass transfers at high current density generally bring about uneven Li nucleation and deposition. This, in turn, leads to a low utilization of the electroactive surface area in 3D current collectors. Besides that, the morphology of plated Li greatly relies on the initial nucleation process, which is critical but remains elusive. To solve the formation of Li dendrites fundamentally, regulating the sites and shape of the plated Li at the initial nucleating stage is an effective approach. Thus, it is imperative to develop a universal technique to manipulate the homogeneous distribution of Li^+ flux above the 3D current framework and regulate the initial nucleation of Li, enabling

Received: September 28, 2018
Published: November 29, 2018

DOI: 10.1021/jacs.8b10488
J. Am. Chem. Soc. XXXX, XXX, XXX−XXX

uniform and dendrite-free Li nucleation and growth even at high current density.

Herein, uniform Li metal nucleation with pancake-like morphology is oriented by a two-step bromide intermediate regulated process. One step is motivated by a Br-doped graphene-like film, which is well integrated with the Cu foam, to regulate homogeneous Li^+ flux and nucleation. Additionally, on the foundation of the uniform nucleation, the morphology of nuclei is further adjusted by CuBr, which reacts with Li and generates LiBr to adjust the formation of pancake-like seeds. Consequently, the nucleation overpotential is significantly reduced at even very high current densities, and the growth of lithium dendrites is effectively suppressed. The Coulombic efficiency of CuBr- and Br-doped graphene-like film modified Cu foam (BGCF) anode can be maintained above 98.8% after over 300 cycles at 2 mA cm^{-2} with a deposition capacity of 2 mA h cm^{-2}. When matching a practical mass loading $LiFePO_4$ (LFP) cathode (up to 20.5 mg cm^{-2}), Li−BGCF||LFP full batteries exhibit excellent cycle performance and a capacity retention of 98% over 200 cycles. These results indicate that conducting the sites and shape of the plated Li at the initial nucleating stage by a two-step combined strategy is an effective approach to build safe Li metal batteries.

RESULTS AND DISCUSSION

Characterization of the BGCF. Compared with bare Cu foam (CF) (Figure S1a−c), the BGCF substrate is tightly covered by a thin film on the surface of CF (Figure 1a) after the surface-assisted Ullmann reaction of hexabromobenzene on the Cu foam. The film, abbreviated as BG, is graphene-like with Br-doping sites and CuBr on the surface and inside.[31−33] The X-ray diffraction (XRD) patterns of CF and BGCF evidence the presence of CuBr in BG (Figure S2a,b). The width of 2.88 Å between neighboring lattice fringes revealed by a high-resolution transmission electron microscopy (HRTEM) image corresponds to (200) planes of CuBr (Figure 1b). The TEM image indicates that the size of CuBr in BGCF is about 40 nm (Figure S3). The surface and cross-sectional energy-dispersive spectroscopy (EDS) maps of BG, as shown in Figure S4a−p, demonstrate uniform C, Br, and Cu element distribution in the film. Thus, CuBr distributes uniformly on the BG. The mass loading of BG (CuBr- and Br-doped graphene-like film) is 5 mg cm^{-2} (6 wt %) in BGCF. Furthermore, the mass fraction of CuBr in BG is 25.6%, which is calculated by inductively coupled plasma. The thickness of the BG is approximately 70 nm (Figure S5a,b). Two major bands in Raman spectroscopy correspond to the presence of a disordered band (D-band) (around 1375 cm^{-1}), representing defects in the graphene layer and in-phase vibration of the graphite lattice band (G-band) (1580 cm^{-1}), respectively (Figure 1c).[34,35] The intensity ratio of the G-band and D-band is 1.04, indicating a large amount of graphene-like structure and defects in BG. In X-ray photoelectron spectroscopy (XPS) (Figure S6), the C 1s signal consists of three peaks, at 284.5, 285.5, and 286 eV, which can be assigned to sp^2-bonded carbon,[33] the C−Br bond and the C−O bond adsorbed from air, respectively (Figure 1d). The main component in the Cu 2p spectrum is Cu^+ (Cu 2p3/2 932.2 eV and Auger spectrum at 572 eV) attributed to CuBr (Figure 1e).[36] The high-resolution Br 3d spectrum (Figure 1f) shows two peaks at 68.2 eV (Br 3d 5/2) and 69.1 eV (Br 3d 3/2), corresponding to the presence of a C−Br bond.[36] The two peaks at 70.2 eV (Br 3d 5/2) and 71.2 eV (Br 3d 3/2) (Figure 1f) are characteristic of the presence of CuBr. These results manifest the coexistence of a C−Br bond and CuBr in the graphene-like film. Compared with the bare Super P, the reduction peak at 2.3 V in the cyclic voltammogram (CV) of CuBr arises from the reaction of CuBr and Li (Figure S7a−d). XPS demonstrates that LiBr is formed after discharge in a Li||Cu battery (Figure S8a−c).

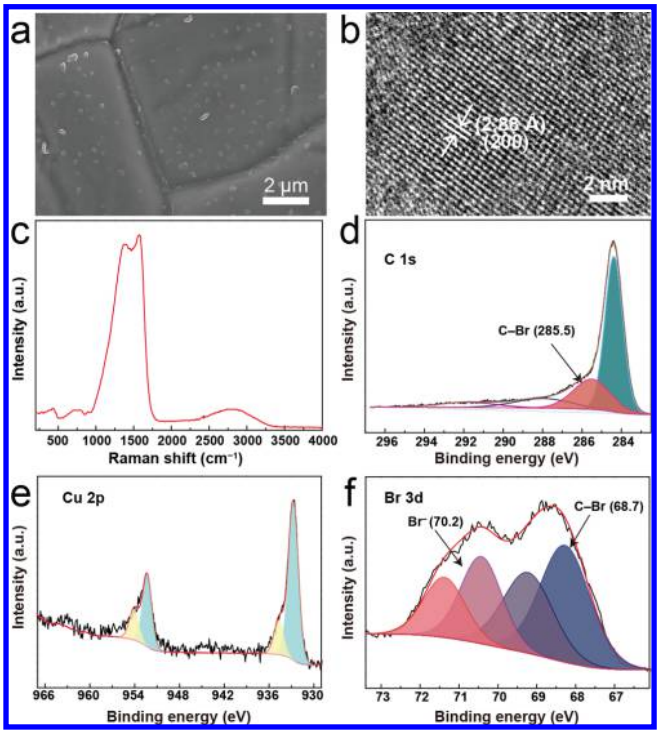

Figure 1. Properties of BG. (a) SEM image of BG-modified Cu foam. (b) HRTEM, (c) Raman, and high-resolution XPS (d) C 1s, (e) Cu 2p, and (f) Br 3d spectra of BG.

Density functional theory (DFT) calculations were conducted to reveal the interaction between nucleated Li and possible nucleation sites. A 14 Å width graphene nanoribbon (GNR) model with 15 Å vacuum in both along the normal direction and the slip direction of GNR was built to simulate the graphene-like carbon film. A single Br-doping site at the edge of the GNR was also considered. The binding energy of the Br-doping site toward a Li atom is −2.06 eV, which is relatively larger than that of pristine graphene, −1.91 eV (Figures 2a,b and S9a−f). Even though the electronegativity of bromine (2.96) is larger than that of carbon (2.55), the filled p orbitals of Br can form a p−π conjugation structure with a carbon plane that feeds back an electron from Br to carbon. As a result, the electron-rich carbon atom near the Br atom can afford a large binding energy toward Lewis-acid Li ions. Differential charge density analyses further confirm the strong interaction between Li and Br-GNR as electron gains between Li and Br/C atoms (Figure S10a and b). Therefore, the large binding energy leads to preferential adsorption, nucleation, and deposition of Li ions on these Br-doping sites.

Besides lithiophilic Br-doping sites, CuBr, which is decorated on the graphene-like film, can even provide a much large binding energy (−4.10 eV) than that of GNR/Br-GNR (Figure 2c). Furthermore, Li prefers to embed in the lattice of CuBr, which indicates that the reaction between Li and CuBr to produce LiBr is thermodynamically and kinetically feasible (Figure S11).[37,38] Therefore, BG is a

DOI: 10.1021/jacs.8b10488
J. Am. Chem. Soc. XXXX, XXX, XXX−XXX

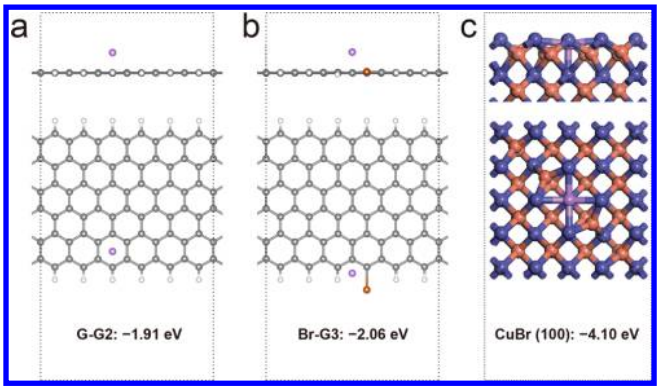

Figure 2. Optimized geometrical structures and corresponding binding energies (E_b) of a Li atom adsorbed on (a) GNR, (b) Br-GNR, and (c) CuBr (100) surface. Gray: C; blue: Br; orange: Cu; purple: Li.

lithiophilic substrate deriving from the interaction between Br-doping sites/CuBr and Li.[39] Moreover, a surface wetting experiment shows that the molten Li can uniformly spread onto the BG, further proving that BG is of excellent lithiophilicity (Figure S12a and b), which coincides with the results of calculation. After LiBr is formed, it can provide a quick Li diffusion pathway with a very low diffusion barrier of around 0.01 eV (Figure S13a and b), agreeing with previous theoretical and experimental reports.[11,40−48] The fast Li diffusion on BG favors a dendrite-free Li plating, which is discussed specifically in the following part.

Morphology of Lithium Metal Deposition. The plating and stripping process of Li on CF and BGCF substrates were investigated in detail at a current density of 2 mA cm^{-2}. Figure S14 shows scanning electron microscopy (SEM) images of lithium metal with increasing Li amounts onto the bare CF. Micrometer-sized Li particles distribute nonuniformly on the skeleton of CF at the initial nucleating stage (Figure S14a and b). These Li particles function as nucleation sites of the subsequent Li deposition as the charges accumulate at these positions in the electric field. As lithium continues to deposit, filaments grow out from the Li particles and expand to sharper, randomly oriented Li dendrites (Figure S14c−j). The plating behavior leads to lower utilization of the electroactive surface area of CF. Moreover, the formed Li dendrites could threaten the safety of batteries by piercing the separator. In the subsequent stripping process, the filaments become slender and sectional (Figure S14k). After recharging to 1 V, a large amount of "dead Li" is left on the CF substrate, inducing an irreversible Li consumption (Figure S14l) and resulting in poor plating/stripping Coulombic efficiency (CE).

In contrast, the shape and site of deposited Li on the BGCF substrate differ significantly from those on the CF. The morphologies of deposited Li with various plating capacities are shown in Figure 3a−i. During discharging, Li ions initially intercalate into the graphene-like film to form a Li/C intercalation compound. When the voltage decreases to below 0 V, the nucleation of Li plating prefers to take place on the BGCF skeleton due to its super lithiophilicity. Meanwhile, the deposited Li reacts with CuBr to form LiBr, which is proved by CV and XPS (Figure S7, S8), achieving a fast Li diffusion pathway on BGCF. At the initial stage of Li deposition with a capacity of 0.3 mA h cm^{-2}, a homogeneous distribution of the pancake-like morphology was observed on the BGCF substrate (Figure 3a). It is attributed to the

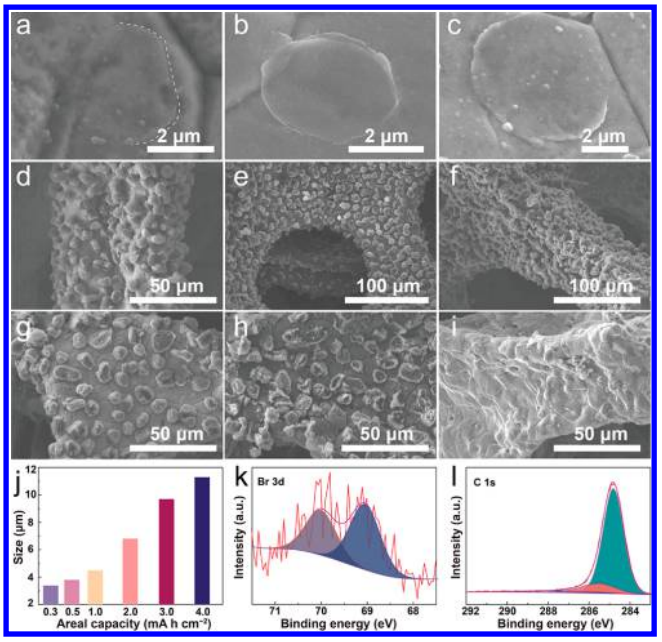

Figure 3. Morphology characterization of lithium metal plating/stripping on the BGCF. SEM images after plating (a) 0.3 mA h cm^{-2}, (b) 0.5 mA h cm^{-2}, (c) 1 mA h cm^{-2}, (d) 2 mA h cm^{-2}, (e) 3 mA h cm^{-2}, and (f) 4 mA h cm^{-2} and stripping (g) 1 mA h cm^{-2}, (h) 2 mA h cm^{-2}, and (i) 4 mA h cm^{-2} (that is, recharged to 1 V) lithium from BGCF. (j) Size of lithium at different areal capacities. XPS of Br 3d (k) and C 1s (l) of BG-modified Cu foil after one cycle (washed with water and alcohol and dried to remove the SEI).

relatively lower diffusion barrier of adjacent LiBr, on which Li ions diffuse easily, distribute uniformly, and aggregate weakly. The uniform pancake-like morphology indicates significantly different Li nucleation behaviors and ensures the formation of a stable solid−electrolyte interphase (SEI) on the Li surface that can restrain the growth of dendrite structures. On increasing the capacity of Li deposition to 0.5 and 1 mA h cm^{-2}, the number of nucleation sites increased, and at the same time, the pancake-like morphology became larger and thicker (Figures 3b and c, S15a−c). In the following plating process, the nucleation sites and size increased and the pancake grew into plump granules even when the capacity reached as high as 4 mA h cm^{-2} (Figures 3d−f, j, S15d−g). Thus, BGCF are able to realize uniform lithium nucleation and preserve a dendrite-free morphology. Moreover, the transformation of disordered dendritic growth to plump granules indicates the fundamental science behind these two behaviors is significantly different. Noticeably, during charging the plated Li can be reversibly stripped from the BGCF without "dead Li". When 1, 2, and 3 mA h cm^{-2} Li was stripped, plump granules conversely transformed into pancake-like Li (Figures 3g and h and S15h). Last, with all 4 mA h cm^{-2} Li being stripped (recharged to 1 V), a clean skeleton reappeared as the pristine state and almost no "dead Li" was left over (Figures 3i, S15i). The C−Br bond can be detected at the fully charged state by XPS (Figure 3k and l), consistent with the calculation results that C−Br bonds are electrochemically stable with Li metal (Figures 2b, S9d−f).

To add weight to the function of the Br-doping site that it can direct uniform nucleation of Li, the BGCF was immersed in diluted hydrochloric acid to remove CuBr, which was proved by XPS (Figure S16). After drying, the BGCF without CuBr was utilized to investigate the plating behavior of Li on Br-doped graphene-like film. Homogeneous nucleation of Li

DOI: 10.1021/jacs.8b10488
J. Am. Chem. Soc. XXXX, XXX, XXX−XXX

was observed after depositing 1 mA h cm^{-2} of Li under the current density of 2 mA cm^{-2}. Nevertheless, the shape of plated Li is similar to that of CF (Figure S17a and b). Furthermore, CuBr-modified Cu foam (CuBr@CF) was prepared as another control sample to highlight the synergistic effect of CuBr- and Br-doped graphene-like film in BGCF (Figure S18a). Interestingly, when plating 2 mA h cm^{-2} Li at 2 mA cm^{-2} on CuBr@CF, a dendrite-free morphology was obtained (Figure S18b,c). This Li deposition behavior is obviously different from that of CF, while similar to that of BGCF. However, the Li depositions are not uniformly distributed on CuBr@CF due to the uncontrolled electric field distribution. Therefore, these two control experiments evidence the synergistic effect of CuBr- and Br-doped graphene-like film in BGCF. These results confirm that the Br-doping site plays an important role in the uniform distribution of nucleated Li particles and the CuBr is indispensable to regulate the morphology of the plated Li. The demonstrated potential of BGCF in controlling uniform Li nucleation and growth behavior shows its superiority in suppressing dendrite growth and opens up an opportunity to improve the CE of metallic Li anodes.

Electrochemical Performance. The electrochemical behavior of CF and BGCF electrodes was examined via galvanostatic discharge/charge voltage profiles in Li||Cu batteries. At current densities of 2, 4, 6, 8, and 10 mA cm^{-2}, the CF electrode exhibits a large Li nucleation overpotential of 61, 57, 78, 93, and 157 mV, respectively, while the BGCF electrode shows remarkably reduced overpotentials of 31, 34, 40, 41, and 84 mV (Figure 4a and b). This can be attributed to the super-lithiophilicity of BGCF. The capacity before Li plating is about 0.2 mA h cm^{-2}, which is due to the formation of LiBr and the inserting of Li in the graphene-like film (Figure 4a). The electrochemical impedance spectroscopy (EIS) was carried out to monitor the evolution of the impedance. The electrolyte resistance (R_e) and the interfacial charge-transfer resistance (R_{ct}) are summarized in Table S1, derived from the EIS in Figure S19.[47] For the Li||CF batteries, the R_e and R_{ct} increase quickly during cycling, indicating severe/continuous depletion of the electrolyte components and formation of byproduct, which damages the electrochemical performance of batteries. In contrast, for BGCF, the R_e remains constant and the R_{ct} decreases during cycling, both of which can be ascribed to the gradually stabilized SEI. Owing to the vital function of the SEI at the electrode/electrolyte interface, it can be assumed that such prominent SEI upon cycling might make for a high CE. To verify this hypothesis, the CEs of the two electrodes were investigated. Fixing the current density at 2.0 mA cm^{-2}, the CE of the CF electrode steadily decreases as cycling progresses, dropping below 90% after 50 and 35 cycles at an areal capacity of 2.0 and 4.0 mA h cm^{-2}, respectively (Figure 4c and d). In comparison, the BGCF electrode demonstrates excellent cycling performance, maintaining a CE of more than 98.8% over 300 cycles at 2.0 mA h cm^{-2} and cycling more than 100 times with a CE of 98% at 4.0 mA h cm^{-2} (Figure 4c and d). Impressively, when the current density was increased to 4 mA cm^{-2}, the BGCF also showed improved and stabilized CE compared with CF (Figure S20a,b). The stable cycling performance at high current density and areal capacity is ascribed to the generation of a stable SEI and high reversible plating/stripping of Li on the BGCF substrate, which stems from the unique pancake-like morphology.

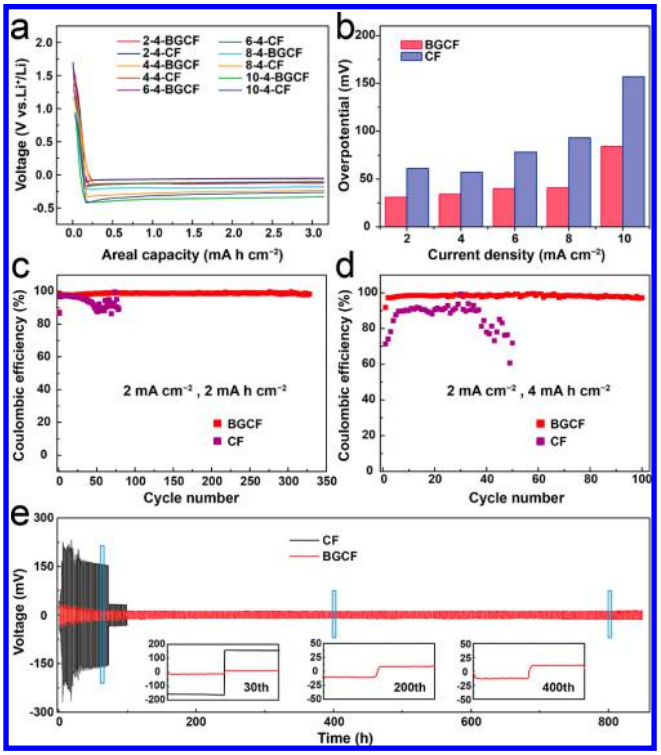

Figure 4. (a) Voltage profiles and (b) the Li nucleation overpotentials on CF and BGCF electrodes at different current densities. (c, d) Comparison in Coulombic efficiency of CF and BGCF at different lithiation capacity. The current density in each cycle is 2 mA cm^{-2}. (e) Voltage−time curves of Li−CF and Li−BGCF in a symmetric cell test at 1 mA cm^{-2} for 1 mA h cm^{-2}.

The long-term interfacial stability of the Li anode was investigated by testing the Li||Li−CF and Li||Li−BGCF symmetric cells. Random voltage oscillations occur in Li||Li−CF cells at 370 h under a current density of 1 mA cm^{-2} caused by the increasing of SEI components and the growth of Li dendrites during Li plating/stripping processes. In comparison, Li||Li−BGCF cells demonstrate a stable voltage during the cycling up to 850 h, exhibiting a stable Li/electrolyte interface and effective suppression of dendrite growth (Figure 4e). The high content of the Br atom, the strong interaction between the Li ion and the Br atom, and the regulation of LiBr jointly result in the relatively uniform Li^+ flux on the BGCF substrate. Hence, an even distribution of Li nucleation and growth on the BGCF substrate are realized, which further contributes to the improved stability of the Li anode.

Further interrogation of BGCF was carried out in Li||LFP full batteries. Areal loading of cathode, Li anode areal capacity utilization, and the charge current densities play crucial roles in the long-term cycling stability of full batteries with high energy and power density.[47−50] Many of the present studies on rate and cycling performance of full batteries are based on low mass loading of cathode and charge current densities. However, in practical application, high cathode loading is applied and more Li are utilized in each deposition/stripping process, which leads to more side reactions along with faster capacity fading. In order to circumvent such restrictions and reflect the real case in practical applications, a high areal capacity cathode matched with limited Li−BGCF of 6 mA h cm^{-2} was used in Li||LFP full batteries. Two different levels of mass loading were investigated: one is an intermediate level of approximate 11.5 mg cm^{-2}, 2 mA h cm^{-2}, and another represents a practical level

DOI: 10.1021/jacs.8b10488
J. Am. Chem. Soc. XXXX, XXX, XXX−XXX

of approximately 20.3 mg cm^{-2}, 3.5 mA h cm^{-2}.[51] The negative/positive (N/P) electrode capacity rates of Li||LFP full batteries with these two levels of cathode loading are 3 and 1.7, respectively. The electrochemical process of the Li||LFP full battery was analyzed by EIS. When the areal capacity of the cathode is 2 mA h cm^{-2}, the EIS curves exhibit a low R_{ct} of 41.6 Ω·cm^2, implying a stable Li/electrolyte interface and well-preserved SEI layer (Figure S21a). The good rate capability of Li||LFP batteries reveals facile ion/electron transport, owing to the uniform Li nucleation, which enables high utilization of the electroactive surface area and largely reduces the local current density (Figure 5a). The battery exhibits excellent long-term

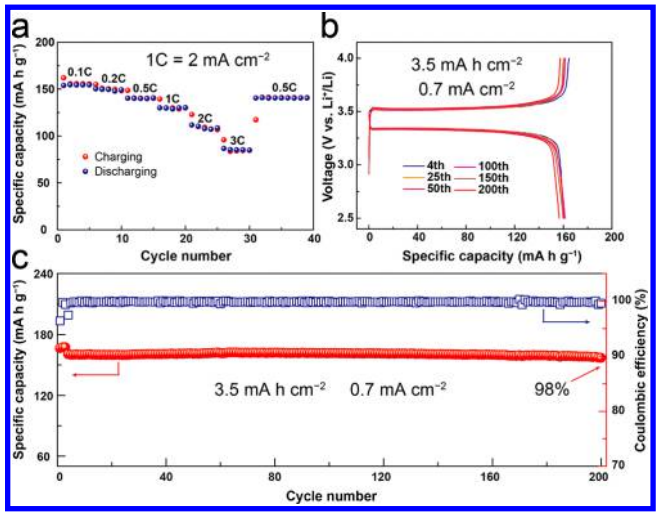

Figure 5. (a) Rate capability of the Li−BGCF anode paired with an LFP cathode at various current densities ranging from 0.2 to 6 mA cm^{-2}. (b) Charge/discharge profiles at different cycle numbers and (c) capacity retention and Coulombic efficiency of a Li−BGCF||LFP full battery with a cathode loading of 3.5 mA h cm^{-2} over 200 cycles at 0.7 mA cm^{-2}.

cycling performance: a cyclability of 94% capacity retention after 400 cycles at a charge/discharge current density up to 1 mA cm^{-2}, which is a relatively high current density of charge (Figure S22).[51] More importantly, it is a big challenge for an anode with limited capacity when the cathode loading is further increased to 3.5 mA h cm^{-2} (20.3 mg cm^{-2}), which calls for a large amount of Li deposition/stripping in each cycle. The full battery still shows a low interfacial charge-transfer resistance of 47.6 Ω·cm^2 (Figure S21b). During cycling, a negligible increase of cell overpotential is observed, indicating that the Li/electrolyte interface is highly stable (Figure 5b) and the full battery maintains a high Columbic efficiency of more than 99.8% (Figure 5c). Remarkably, an excellent cyclability of 98% capacity retention after 200 cycles is achieved at a charge/discharge current density of 0.7 mA cm^{-2} (Figure 5c). Such improved cycling performance at high cathode loading indicates higher utilization of Li in the Li−BGCF anode, benefiting from the stable SEI, high reversible Li plating/stripping process, and facile ion/electron transport. These outstanding performances of the full battery with a high cathode loading reveal the Li−BGCF anode is close to appropriate for practical battery systems.

Mechanism of Uniform Li Nucleation with Pancake-like Morphology in the BGCF. Herein, the uniform nucleation and dendrite-free growth of Li originate from the two-step synergy process regulated by C−Br bonds and CuBr. A schematic diagram of graphene-like film modified by Br-doping and CuBr-decoration is illustrated in Figure 6a based

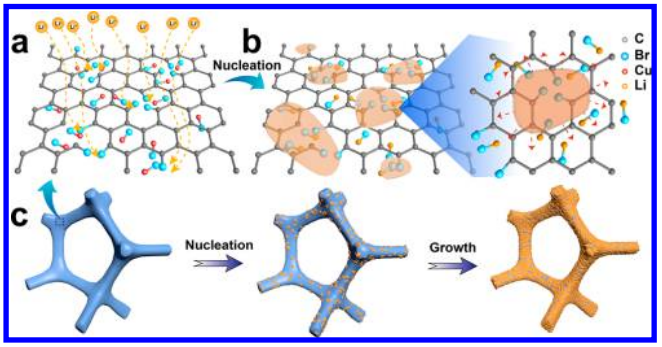

Figure 6. Schematics of Li metal deposition on BGCF. (a) Homogeneous Li$^+$ flux above Br-doped graphene-like film and CuBr. (b) CuBr transformed into LiBr during Li plating. Selective deposition of Li metal on Br-doping sites and the nearby LiBr regulate Li metal nucleation into a pancake-like morphology of Li seeds. Gray, blue, red, and orange represent C, Br, Cu, and Li, respectively. (c) Nucleation and growth process of Li metal on BGCF.

on the preparation and the analysis above. Br-doping and CuBr uniformly distribute on the surface of the electrode. Importantly, the high binding energy of Br-doping sites and Li atoms endows the BG with excellent lithiophilicity to strongly adsorb Li$^+$ and further induce uniform Li nucleation. On the bases of the uniform nucleation, both experiments and theoretical calculations have effectively established that CuBr can react with Li metal to form LiBr, which provides a fast Li diffusion pathway and further regulates the growth of Li atoms into pancake-like rather than whisker Li (Figure 6b).[46] Consequently, uniform nucleation and dendrite-free growth of Li is realized in the 3D conductive framework (Figure 6c). The enhanced lithiophilicity renders the reduced Li nucleation overpotential under high current densities. The pancake-like morphology stabilizes the SEI layer, thus reducing side reactions between the electrolyte and Li metal. As a result, the CE of BGCF was significantly improved and the Li metal batteries with extremely high cathode loading displayed excellent cycling performance.

■ CONCLUSIONS

In summary, bromide intermediates have been proposed that enable homogeneous Li nuclei distribution and dendrite-free growth in 3D conducting skeletons. A graphene-like film with Br-doping and CuBr is well integrated with Cu foam. The strong interaction between Li and Br-doping sites guides uniform Li$^+$ flux over a Br-doped graphene-like film and hence conducts a uniform Li nucleation. Moreover, CuBr can react with Li to form LiBr, which can provide a fast Li diffusion pathway to adjust Li seeds in a pancake-like morphology. With the regulation of LiBr and Br-doping, BGCF effectively guides Li nucleation in pancake-like seeds and growth into granular Li metal and improves the Coulombic efficiency of Li metal cycling under a high current density (more than 98.8% for over 300 cycles at 2.0 mA cm^{-2} and 2.0 mA h cm^{-2}). The stable cycling of 850 h is achieved in the Li||Li−BGCF symmetrical cell. More importantly, by virtue of a highly reversible Li plating/stripping process, the full battery maintained more than 94% of the initial capacity after 400 cycles and a capacity retention of 98% after 200 cycles with a high cathode loading

DOI: 10.1021/jacs.8b10488
J. Am. Chem. Soc. XXXX, XXX, XXX−XXX

of 2 mA h cm^{-2} and 3.5 mA h cm^{-2}, respectively. Accordingly, the two-step synergy through bromide intermediates or other halogenides (such as chloride, iodide, etc.) might be a sensible strategy to provide Li metal with opportunities for the application of safe and stable high energy density batteries.

■ ASSOCIATED CONTENT

Supporting Information

The Supporting Information is available free of charge on the ACS Publications website at DOI: 10.1021/jacs.8b10488.

More details on experimental and characterizations; additional SEM, XRD, TEM EDS images, XPS, CV curves, phase diagram, digital photo, electrochemical impedance plots, theoretical simulations, and cyclic performance (PDF)

■ AUTHOR INFORMATION

Corresponding Authors

*ygguo@iccas.ac.cn
*ljiang@iccas.ac.cn
*wanlijun@iccas.ac.cn

ORCID

Xiang Chen: 0000-0002-7686-6308
Ji-Lei Shi: 0000-0003-2887-2620
Ya-Xia Yin: 0000-0002-0983-9916
Qiang Zhang: 0000-0002-3929-1541
Yu-Guo Guo: 0000-0003-0322-8476
Li-Jun Wan: 0000-0002-0656-0936

Author Contributions

⊥H. Duan, J. Zhang, and X. Chen contributed equally to this paper.

Notes

The authors declare no competing financial interest.

■ ACKNOWLEDGMENTS

This work was supported by the Basic Science Center Project of National Natural Science Foundation of China (Grant No. 51788104), the National Key R&D Program of China (Grant No. 2016YFA0202500), the National Natural Science Foundation of China (Grant Nos. 51772301 and 21773264), the "Transformational Technologies for Clean Energy and Demonstration", Strategic Priority Research Program of the Chinese Academy of Sciences (Grant No. XDA 21070300), and Hundred Talents Plan of Chinese Academy of Sciences, the Strategic Priority Research Program of Chinese Academy of Sciences (Grant No. XDB30000000). The authors acknowledged the support from Tsinghua National Laboratory for Information Science and Technology for theoretical simulations. The authors thank Xinan Yang for the STEM support.

■ REFERENCES

(1) Tarascon, J. M.; Armand, M. Issues and challenges facing rechargeable lithium batteries. *Nature* **2001**, *414*, 359.
(2) Xu, W.; Wang, J.; Ding, F.; Chen, X.; Nasybulin, E.; Zhang, Y.; Zhang, J.-G. Lithium metal anodes for rechargeable batteries. *Energy Environ. Sci.* **2014**, *7*, 513.
(3) Xin, S.; Gu, L.; Zhao, N.-H.; Yin, Y.-X.; Zhou, L.-J.; Guo, Y.-G.; Wan, L.-J. Smaller Sulfur Molecules Promise Better Lithium−Sulfur Batteries. *J. Am. Chem. Soc.* **2012**, *134*, 18510.
(4) Bruce, P. G.; Freunberger, S. A.; Hardwick, L. J.; Tarascon, J.-M. Li−O2 and Li−S batteries with high energy storage. *Nat. Mater.* **2011**, *11*, 19.
(5) Lin, D.; Liu, Y.; Cui, Y. Reviving the lithium metal anode for high-energy batteries. *Nat. Nanotechnol.* **2017**, *12*, 194.
(6) Kim, H.; Jeong, G.; Kim, Y.-U.; Kim, J.-H.; Park, C.-M.; Sohn, H.-J. Metallic anodes for next generation secondary batteries. *Chem. Soc. Rev.* **2013**, *42*, 9011.
(7) Lu, D.; Shao, Y.; Lozano, T.; Bennett, W. D.; Graff, G. L.; Polzin, B.; Zhang, J.; Engelhard, M. H.; Saenz, N. T.; Henderson, W. A.; Bhattacharya, P.; Liu, J.; Xiao, J. Failure Mechanism for Fast-Charged Lithium Metal Batteries with Liquid Electrolytes. *Adv. Energy Mater.* **2015**, *5*, 1400993.
(8) Harry, K. J.; Hallinan, D. T.; Parkinson, D. Y.; MacDowell, A. A.; Balsara, N. P. Detection of subsurface structures underneath dendrites formed on cycled lithium metal electrodes. *Nat. Mater.* **2014**, *13*, 69.
(9) Yang, C. P.; Fu, K.; Zhang, Y.; Hitz, E.; Hu, L. B. Protected Lithium-Metal Anodes in Batteries: From Liquid to Solid. *Adv. Mater.* **2017**, *29*, 28.
(10) Ding, F.; Xu, W.; Graff, G. L.; Zhang, J.; Sushko, M. L.; Chen, X.; Shao, Y.; Engelhard, M. H.; Nie, Z.; Xiao, J.; Liu, X.; Sushko, P. V.; Liu, J.; Zhang, J.-G. Dendrite-Free Lithium Deposition via Self-Healing Electrostatic Shield Mechanism. *J. Am. Chem. Soc.* **2013**, *135*, 4450.
(11) Cheng, X.-B.; Zhao, M.-Q.; Chen, C.; Pentecost, A.; Maleski, K.; Mathis, T.; Zhang, X.-Q.; Zhang, Q.; Jiang, J.; Gogotsi, Y. Nanodiamonds suppress the growth of lithium dendrites. *Nat. Commun.* **2017**, *8*, 336.
(12) Li, W.; Yao, H.; Yan, K.; Zheng, G.; Liang, Z.; Chiang, Y.-M.; Cui, Y. The synergetic effect of lithium polysulfide and lithium nitrate to prevent lithium dendrite growth. *Nat. Commun.* **2015**, *6*, 7436.
(13) Kanamura, K.; Shiraishi, S.; Takehara, Z. i. Electrochemical Deposition of Very Smooth Lithium Using Nonaqueous Electrolytes Containing HF. *J. Electrochem. Soc.* **1996**, *143*, 2187.
(14) Lu, Y.; Tu, Z.; Archer, L. A. Stable lithium electrodeposition in liquid and nanoporous solid electrolytes. *Nat. Mater.* **2014**, *13*, 961.
(15) Zheng, G.; Lee, S. W.; Liang, Z.; Lee, H.-W.; Yan, K.; Yao, H.; Wang, H.; Li, W.; Chu, S.; Cui, Y. Interconnected hollow carbon nanospheres for stable lithium metal anodes. *Nat. Nanotechnol.* **2014**, *9*, 618.
(16) Kozen, A. C.; Lin, C.-F.; Pearse, A. J.; Schroeder, M. A.; Han, X.; Hu, L.; Lee, S.-B.; Rubloff, G. W.; Noked, M. Next-Generation Lithium Metal Anode Engineering via Atomic Layer Deposition. *ACS Nano* **2015**, *9*, 5884.
(17) Li, N.-W.; Shi, Y.; Yin, Y.-X.; Zeng, X.-X.; Li, J.-Y.; Li, C.-J.; Wan, L.-J.; Wen, R.; Guo, Y.-G. Smart Solid Electrolyte Interphase Layer for Long Life Lithium Metal Anodes. *Angew. Chem., Int. Ed.* **2018**, *57*, 1505.
(18) Suo, L.; Hu, Y.-S.; Li, H.; Armand, M.; Chen, L. A new class of Solvent-in-Salt electrolyte for high-energy rechargeable metallic lithium batteries. *Nat. Commun.* **2013**, *4*, 1481.
(19) Qian, J.; Henderson, W. A.; Xu, W.; Bhattacharya, P.; Engelhard, M.; Borodin, O.; Zhang, J.-G. High rate and stable cycling of lithium metal anode. *Nat. Commun.* **2015**, *6*, 6362.
(20) Liu, W.; Lee, S. W.; Lin, D.; Shi, F.; Wang, S.; Sendek, A. D.; Cui, Y. Enhancing ionic conductivity in composite polymer electrolytes with well-aligned ceramic nanowires. *Nat. Energy* **2017**, *2*, 17035.
(21) Choudhury, S.; Mangal, R.; Agrawal, A.; Archer, L. A. A highly reversible room-temperature lithium metal battery based on crosslinked hairy nanoparticles. *Nat. Commun.* **2015**, *6*, 10101.
(22) Fu, K.; Gong, Y.; Dai, J.; Gong, A.; Han, X.; Yao, Y.; Wang, C.; Wang, Y.; Chen, Y.; Yan, C.; Li, Y.; Wachsman, E. D.; Hu, L. Flexible, solid-state, ion-conducting membrane with 3D garnet nanofiber networks for lithium batteries. *Proc. Natl. Acad. Sci. U. S. A.* **2016**, *113*, 7094.
(23) Zeng, X.-X.; Yin, Y.-X.; Li, N.-W.; Du, W.-C.; Guo, Y.-G.; Wan, L.-J. Reshaping Lithium Plating/Stripping Behavior via Bifunctional Polymer Electrolyte for Room-Temperature Solid Li Metal Batteries. *J. Am. Chem. Soc.* **2016**, *138*, 15825.
(24) Duan, H.; Yin, Y.-X.; Shi, Y.; Wang, P.-F.; Zhang, X.-D.; Yang, C.-P.; Shi, J.-L.; Wen, R.; Guo, Y.-G.; Wan, L.-J. Dendrite-Free Li-

DOI: 10.1021/jacs.8b10488
J. Am. Chem. Soc. XXXX, XXX, XXX−XXX

Metal Battery Enabled by a Thin Asymmetric Solid Electrolyte with Engineered Layers. *J. Am. Chem. Soc.* **2018**, *140*, 82.
(25) Yang, C. P.; Zhang, L.; Liu, B. Y.; Xu, S. M.; Hamann, T.; McOwen, D.; Dai, J. Q.; Luo, W.; Gong, Y. H.; Wachsman, E. D.; Hu, L. B. Continuous plating/stripping behavior of solid-state lithium metal anode in a 3D ion-conductive framework. *Proc. Natl. Acad. Sci. U. S. A.* **2018**, *115*, 3770.
(26) Schneider, N. M.; Park, J. H.; Grogan, J. M.; Steingart, D. A.; Bau, H. H.; Ross, F. M. Nanoscale evolution of interface morphology during electrodeposition. *Nat. Commun.* **2017**, *8*, 2174.
(27) Yang, C.-P.; Yin, Y.-X.; Zhang, S.-F.; Li, N.-W.; Guo, Y.-G. Accommodating lithium into 3D current collectors with a submicron skeleton towards long-life lithium metal anodes. *Nat. Commun.* **2015**, *6*, 8058.
(28) Yun, Q.; He, Y.-B.; Lv, W.; Zhao, Y.; Li, B.; Kang, F.; Yang, Q.-H. Chemical Dealloying Derived 3D Porous Current Collector for Li Metal Anodes. *Adv. Mater.* **2016**, *28*, 6932.
(29) Zhang, Y.; Liu, B.; Hitz, E.; Luo, W.; Yao, Y.; Li, Y.; Dai, J.; Chen, C.; Wang, Y.; Yang, C.; Li, H.; Hu, L. A carbon-based 3D current collector with surface protection for Li metal anode. *Nano Res.* **2017**, *10*, 1356.
(30) Liu, W.; Lin, D.; Pei, A.; Cui, Y. Stabilizing Lithium Metal Anodes by Uniform Li-Ion Flux Distribution in Nanochannel Confinement. *J. Am. Chem. Soc.* **2016**, *138*, 15443.
(31) Chen, M.; Xiao, J.; Steinrück, H.-P.; Wang, S.; Wang, W.; Lin, N.; Hieringer, W.; Gottfried, J. M. Combined Photoemission and Scanning Tunneling Microscopy Study of the Surface-Assisted Ullmann Coupling Reaction. *J. Phys. Chem. C* **2014**, *118*, 6820.
(32) Gutzler, R.; Walch, H.; Eder, G.; Kloft, S.; Heckl, W. M.; Lackinger, M. Surface mediated synthesis of 2D covalent organic frameworks: 1,3,5-tris(4-bromophenyl)benzene on graphite(001), Cu(111), and Ag(110). *Chem. Commun.* **2009**, *0*, 4456.
(33) Cai, J.; Ruffieux, P.; Jaafar, R.; Bieri, M.; Braun, T.; Blankenburg, S.; Muoth, M.; Seitsonen, A. P.; Saleh, M.; Feng, X.; Müllen, K.; Fasel, R. Atomically precise bottom-up fabrication of graphene nanoribbons. *Nature* **2010**, *466*, 470.
(34) Gupta, A.; Chen, G.; Joshi, P.; Tadigadapa, S.; Eklund. Raman Scattering from High-Frequency Phonons in Supported n-Graphene Layer Films. *Nano Lett.* **2006**, *6*, 2667.
(35) Kudin, K. N.; Ozbas, B.; Schniepp, H. C.; Prud'homme, R. K.; Aksay, I. A.; Car, R. Raman Spectra of Graphite Oxide and Functionalized Graphene Sheets. *Nano Lett.* **2008**, *8*, 36.
(36) Haikal, R. R.; Soliman, A. B.; Amin, M.; Karakalos, S. G.; Hassan, Y. S.; Elmansi, A. M.; Hafez, I. H.; Berber, M. R.; Hassanien, A.; Alkordi, M. H. Synergism of carbon nanotubes and porous-organic polymers (POPs) in CO2 fixation: One-pot approach for bottom-up assembly of tunable heterogeneous catalyst. *Appl. Catal., B* **2017**, *207*, 347.
(37) Ong, S. P.; Wang, L.; Kang, B.; Ceder, G. Li−Fe−P−O2 Phase Diagram from First Principles Calculations. *Chem. Mater.* **2008**, *20*, 1798.
(38) Jain, A.; Hautier, G.; Ong, S. P.; Moore, C. J.; Fischer, C. C.; Persson, K. A.; Ceder, G. Formation enthalpies by mixing GGA and GGA calculations. *Phys. Rev. B: Condens. Matter Mater. Phys.* **2011**, *84*, 045115.
(39) Zhang, R.; Chen, X.-R.; Chen, X.; Cheng, X.-B.; Zhang, X.-Q.; Yan, C.; Zhang, Q. Lithiophilic Sites in Doped Graphene Guide Uniform Lithium Nucleation for Dendrite-Free Lithium Metal Anodes. *Angew. Chem., Int. Ed.* **2017**, *56*, 7764.
(40) Uthaisar, C.; Barone, V. Edge effects on the characteristics of li diffusion in graphene. *Nano Lett.* **2010**, *10*, 2838.
(41) Zhou, L.-J.; Hou, Z. F.; Wu, L.-M. First-Principles Study of Lithium Adsorption and Diffusion on Graphene with Point Defects. *J. Phys. Chem. C* **2012**, *116*, 21780.
(42) Fan, X.; Zheng, W. T.; Kuo, J. L. Adsorption and diffusion of Li on pristine and defective graphene. *ACS Appl. Mater. Interfaces* **2012**, *4*, 2432.
(43) Kishida, I.; Koyama, Y.; Kuwabara, A.; Yamamoto, T.; Oba, F.; Tanaka, I. First-Principles Calculations of Migration Energy of Lithium Ions in Halides and Chalcogenides. *J. Phys. Chem. B* **2006**, *110*, 8258.
(44) Koyama, Y.; Yamada, Y.; Tanaka, I.; Nishitani, S. R.; Adachi, H.; Murayama, M.; Kanno, R. Evaluation of Migration Energy of Lithium Ions in Chalcogenides and Halides by First Principles Calculation. *Mater. Trans.* **2002**, *43*, 1460.
(45) Choudhury, S.; Wei, S.; Ozhabes, Y.; Gunceler, D.; Zachman, M. J.; Tu, Z.; Shin, J. H.; Nath, P.; Agrawal, A.; Kourkoutis, L. F.; Arias, T. A.; Archer, L. A. Designing solid-liquid interphases for sodium batteries. *Nat. Commun.* **2017**, *8*, 898.
(46) Ozhabes, Y.; Gunceler, D.; Arias, T. A. Stability and surface diffusion at lithium-electrolyte interphases with connections to dendrite suppression. *arXiv preprint arXiv* **2015**, *1504*, 05799.
(47) Zheng, J.; Engelhard, M. H.; Mei, D.; Jiao, S.; Polzin, B. J.; Zhang, J.-G.; Xu, W. Electrolyte additive enabled fast charging and stable cycling lithium metal batteries. *Nat. Energy* **2017**, *2*, 17012.
(48) Jiao, S.; Zheng, J.; Li, Q.; Li, X.; Engelhard, M. H.; Cao, R.; Zhang, J.-G.; Xu, W. Behavior of Lithium Metal Anodes under Various Capacity Utilization and High Current Density in Lithium Metal Batteries. *Joule* **2018**, *2*, 110.
(49) Sun, H.; Mei, L.; Liang, J.; Zhao, Z.; Lee, C.; Fei, H.; Ding, M.; Lau, J.; Li, M.; Wang, C.; Xu, X.; Hao, G.; Papandrea, B.; Shakir, I.; Dunn, B.; Huang, Y.; Duan, X. Three-dimensional holey-graphene/niobia composite architectures for ultrahigh-rate energy storage. *Science* **2017**, *356*, 599.
(50) Ye, H.; Xin, S.; Yin, Y.-X.; Li, J.-Y.; Guo, Y.-G.; Wan, L.-J. Stable Li Plating/Stripping Electrochemistry Realized by a Hybrid Li Reservoir in Spherical Carbon Granules with 3D Conducting Skeletons. *J. Am. Chem. Soc.* **2017**, *139*, 5916.
(51) Liu, B.; Zhang, J.-G.; Xu, W. Advancing Lithium Metal Batteries. *Joule* **2018**, *2*, 833.

DOI: 10.1021/jacs.8b10488
J. Am. Chem. Soc. XXXX, XXX, XXX−XXX